



# Ballast crushing probability model considering the influence of particle morphology and size

Rui Gao<sup>1</sup> · Zhiwen Yuan<sup>1</sup> · Qihang Hu<sup>1</sup> · Jing Chen<sup>2</sup>

Received: 3 November 2023 / Accepted: 12 February 2024 / Published online: 20 March 2024  
© The Author(s), under exclusive licence to Springer-Verlag GmbH Germany, part of Springer Nature 2024

## Abstract

The non-uniform shape and diverse dimensions exert a substantial influence on the distribution of forces within the ballast, hence affecting its bearing capacity. The objective of this work was to investigate the interrelated impact of particle shape and size on ballast strength, and then construct a prediction model that could estimate the chance of ballast crushing. For these purposes, both three-dimensional scanning and single-particle compression tests were undertaken. The morphology of ballast particles at various scales was comprehensively characterized by computing diverse parameters based on the scanning results. The present study systematically assessed the impact of size, overall shape and roundness on particle crushing behavior and parameters. Then a novel approach was introduced to calculate characteristic strength, taking into account the influence of particle morphology. A ballast crushing probability distribution model was established, which incorporated the Weibull model. The anticipation of ballast crushing probabilities can be achieved within this framework by analyzing particle size and morphology parameters. At last, the actual crushing probabilities were compared to the predicted probabilities for a sample of 50 randomly chosen ballasts. The results revealed that 80% of the particles displayed a deviation of less than 10%, which proved the accuracy of the applied method.

**Keywords** Crushing probability model · Ballast strength · Particle morphology analysis · Single particle compression · Three-dimensional scanning

## 1 Introduction

The degradation of ballast occurs over extended periods of usage as a result of the impact of upper loads. The degradation of the subgrade has a direct impact on its load-bearing capacity and ability to absorb shocks, which in turn affects

the safety and comfort of railway operations. Therefore, it is crucial to perform routine maintenance on the ballast bed [1, 2]. To offer theoretical guidance for this maintenance, it becomes essential to investigate how ballast responds to external forces, particularly its crushing behavior. The crushing strength of ballast is a pivotal determinant of its load-bearing capacity and serves as a crucial parameter for studying its crushing process. The comprehensive performance of a large quantity of ballast can be assessed by determining the crushing probability of particles within the ballast group under various stress conditions. This is achieved by calculating the particle crushing strength [3–5]. Owing to its genesis through the random fragmentation of solid rock, ballast exhibits inherent variability in terms of particle size and shape. The objective of this study is to conduct a comprehensive analysis of the influence of shape and size attributes of ballast on its performance. Through this analysis, we seek to uncover underlying patterns, enabling us to predict ballast crushing probabilities without the need for direct crushing tests. This endeavor carries practical significance in the realm of ballast technology's practical application.

---

✉ Rui Gao  
gaorui@whu.edu.cn; gauryru@163.com  
Zhiwen Yuan  
yuanzhiwen@whu.edu.cn; zwyuanwhu@163.com  
Qihang Hu  
huqihang@whu.edu.cn; huqihang01@qq.com  
Jing Chen  
j.chen9412@zju.edu.cn

<sup>1</sup> The Key Laboratory of Safety for Geotechnical and Structural Engineering of Hubei Province, School of Civil Engineering, Wuhan University, Wuhan 430072, China

<sup>2</sup> Department of Civil Engineering, Zhejiang University, Hangzhou 310058, China

Extensive research has been conducted on the size effect of geotechnical particles. Scholars have carried out various investigations using methods such as single particle compression tests [6, 7], one-dimensional compression tests [8], large triaxial tests [9], and straight shear tests [10, 11]. In the domain of one-dimensional compression tests, Xiao made an observation regarding the reduction in yield stress of sandstone particles as their size decreased [12]. Zhou's work revealed that particle compressive strength adhered to the Weibull distribution, with the characteristic strength displaying an exponential relationship with particle size [13]. The numerical simulations conducted by Zhao have revealed a correlation between the size effect observed in stacked stone particles and the distribution of defects within them [14]. The influence of particle morphology on the crushing process is mediated through force states, prompting numerous studies to consider particle shape factors [15, 16]. Aman explored the dependence of irregular particle crushing probability on energy and force, proposing a lognormal cumulative distribution fit [17]. Kim proposed a novel abrasion assessment model that is based on shape indexes. This model integrates image processing techniques and Los Angeles abrasion tests, while also taking into consideration the shapes of particles [18]. Regarding abrasion resistance, Xu identified the impact of particle shape on ballast, noting that needle and flake-shaped ballast are more prone to breaking than conventional shapes [19]. In a study conducted by Guo, a quantitative evaluation was performed to analyze the morphology of particle damage. The findings emphasized that particles with a flaky or elongated shape are more prone to experiencing volume loss and corner breakage [20]. Separate direct shear tests by Jing [21] and Danesh [22] showcased the influence of single particle ballast morphology on aggregate shear strength. The incorporation of descriptive parameters for complex particle shapes in previous studies [5, 23–25] has been limited when it comes to analyzing the impact of morphology on the crushing process. The existing body of research has primarily focused on investigating the impact of morphology on the properties of ballast aggregates. However, the influence of particle morphology on the crushing strength and probability of individual ballast grains remains an area that has not been thoroughly examined. Although it is more realistic to study the stress condition of single-particle ballast in aggregate tests, it is very limited in monitoring the mechanical response and crushing behavior of individual particles, therefore, this paper adopts the uniaxial compression test and tries to provide a quantitative method to analyze the crushing pattern of ballast affected by morphology and size, starting from the simple stress state. Single particle uniaxial compression test has been widely used in the study of

particle crushing strength and crushing probability, and this test can obtain the key mechanical response as well as crushing characteristics of single particles [6, 7, 13].

The Weibull statistical distribution function is a well-established tool used to establish a relationship between the probability of damage and the strength of brittle materials. It provides a way to comprehend the level of discreteness in strength, where higher values of the Weibull modulus indicate a greater degree of discreteness [26]. This distribution function has found utility in depicting the interplay between ballast particle crushing probability and characteristic strength, producing commendable outcomes [3, 27]. However, the Weibull distribution is limited in its ability to accurately predict the probability of individual ballast grain crushing events, despite its ability to provide insights into the overall trend of ballast strength across a large number of particles. Moreover, McDowell's findings underscore the significance of material shape similarity when applying the Weibull distribution to assess the strength of brittle particles like ballast [28]. The aforementioned requirement was fulfilled by previous researchers through the utilization of ballast particles that possessed regular shapes. The potential for expanding the Weibull distribution to incorporate ballast particles with diverse morphological parameters has yet to be investigated.

This study involved a comprehensive methodology that involved refining the 3D geometry of ballast particles and conducting single-particle compression testing. The acquisition of parameters for quantitatively characterizing the overall shape and roundness of particles was accomplished using programmed techniques. Subsequently, the impact of particle morphology and size on ballast crushing behavior and parameters was thoroughly examined. An innovative approach for determining characteristic strength, incorporating the morphological characteristics of ballast, was presented. Additionally, a sophisticated fragmentation probability distribution model was formulated, which takes into account particle shape considerations.

## 2 Experimental design

### 2.1 Materials

The test material utilized in this study consisted of granite gravel obtained from a quarry located in Wuhan, China. According to the Chinese ballast standard (TB/T 2140–2008), the ballast grading requirements are shown in Fig. 1, and a number of particles were randomly selected from granite crushed stone as the fresh ballast for the test, which ranged from 16 to 63 mm. This is in accordance with the ballast standard (TB/T 2140–2008) and has been applied in previous studies [10, 16]. The collected ballast was

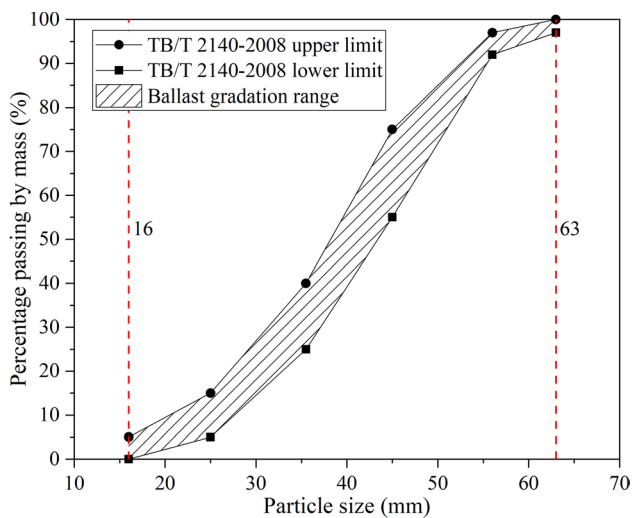


**Fig. 1** First-class railroad ballast grain size grading standard in (TB/T 2140-2008)

**Table 1** Ballast materials group

Serial number	1	2	3	4	5
Particle size range /mm	56–63	45–56	35.5–45	25–35.5	16–25

segregated into five distinct groups based on particle size in accordance with the Chinese ballast standard. Employing a square hole sieve, the categorization was achieved, as outlined in Table 1, where the particle size was defined by the side length of the square hole. Previous studies conducted by Mcdowell and Amon have confirmed that utilizing 30 test data sets is an adequate approach for characterizing the average strength and strength distribution within a particular size range [28]. In order to ensure alignment, our study employed a random selection process to choose 40 ballasts from each group. After the selection process, the ballasts were subjected to a comprehensive cleaning and drying protocol. Subsequently, their mass was determined by employing an electronic scale with a precision level of 0.01 g. Based on the stochastic selection of ballast particles within each group, it can be inferred that these samples possess statistical representativeness of the characteristics of their respective groups. In addition to the particle morphology and size considered in this paper, the fragmentation and breakage of ballast depends on the type of parent rock and the stress state of the parent rock as it breaks into ballast, so the fresh ballast used in the tests was all crushed from the same batch of granite, thus ensuring consistent type and stress stage of the parent rock. The particle morphology and size can be clearly studied. The test material conforms to the Chinese ballast specification and is representative of granite ballast, which is widely used in China.

## 2.2 Methods

Figure 2a depicts the ballast shape, which was thoroughly scanned utilizing the chunk scanning feature of a high-precision 3D scanner. In order to achieve thorough coverage, the ballast was subjected to multiple reorientations during the scanning process, effectively encompassing all facets and corners. The point cloud model was created by smoothly merging the feature points found in overlapping regions. The precision of the acquisition method is demonstrated by a maximum point cloud offset of less than 0.03 mm.

During single-particle compression test, precise positioning was performed, ensuring that the particles were placed on the lower plate in such a way that their long-axis plane was almost parallel to both the upper and lower plates. The implementation of this positioning strategy enables the particles to establish consistent contact with the lower plate at multiple locations, thereby guaranteeing their stability throughout the loading process. Following this, the upper plate was systematically and progressively lowered until it made contact with the particles. The initial distance between the plates was recorded as the reference point for the compression test. The test adopts the displacement loading method, employing a computerized servo control mechanism, and the upper plate was then subjected to quasi-static loading at a rate of 1 mm/min. During this process, sensors integrated into the upper plate collected reaction force and displacement data at a frequency of 10 Hz. Simultaneously, two high-speed cameras were strategically positioned, capturing the loading process from both front and rear angles to facilitate the assessment of particle loading conditions, as depicted in Fig. 2b. The loading process was considered complete when there was a significant decrease in the load–displacement curve and the dislodging of debris from particles that accounted for more than one-third of the total initial particle mass [3]. The observed phenomenon suggests that the particles have experienced a loss in their ability to maintain their strength properties as a result of the loss of mass, indicating a process of particle fragmentation. As a result, the loading process was stopped at this point. The above loading process was then repeated for each of the 200 selected particles, and the loading process for each particle was carried out individually and consecutively until overall crushing occurred. Studies have been carried out using similar test methods to research the crushing of single-grained rocks [5, 12, 16, 17], which proves the validity of the method.

The point cloud model of ballast, the load–displacement curve during compression of ballast single particles, and the particle crushing condition were obtained through the test.

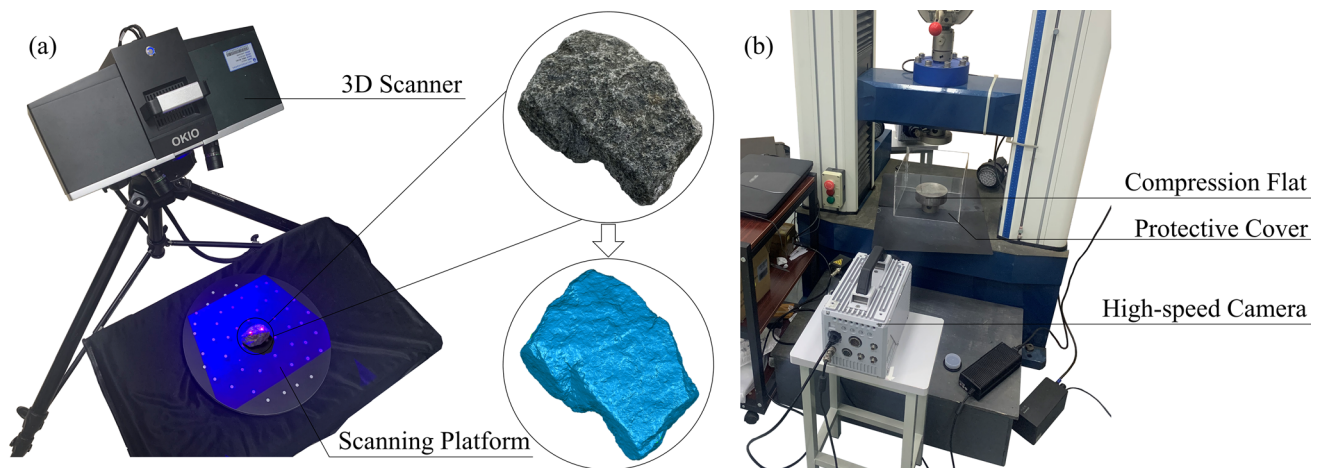


Fig. 2 Test equipment **a** three-dimensional scanning test; **b** single particle compression test

### 3 Crushing probability model construction

#### 3.1 Description of particle morphology

The characterization of ballast particle morphology has traditionally relied on three main scales: form, roundness, and surface texture. These scales were initially introduced by Wadell [23]. However, considering the limited impact of surface texture on the strength of individual particles—primarily affecting friction properties—our focus here centers on form and roundness. Researchers have proposed numerous morphological descriptors. Previous methodologies, which were limited in their ability to acquire morphology, primarily resulted in the derivation of parameters in two dimensions. Yet, with the maturation of 3D scanning technology and CT tomography, efficient acquisition of three-dimensional models for irregular particles has been realized. As a result, there have been proposed parameters that can capture the complete three-dimensional morphology. This helps to address the issue of randomness in two-dimensional descriptors caused by variations in projection angles. Table 2 presents a compilation of the description parameters.

For the purpose of being able to comprehensively assess the overall shape of the ballast, we introduce the regular shape index,  $S_r$ , which takes into account both the elongation ratio and flatness ratio. These two ratios represent different particle tendencies towards specific shapes and are independent indicators. The regular shape index,  $S_r$ , is expressed by Eq. (1):

$$S_r = 1 - (1 - EI)^2 - (1 - FI)^2 \quad (1)$$

Here the elongation ratio,  $EI$ , is defined as the ratio of the short axis length ( $S$ ) to the intermediate axis length ( $I$ ), and

the flatness ratio,  $FI$ , is the ratio of the intermediate axis length ( $I$ ) to the longest axis length ( $L$ ). The  $S_r$  value in Fig. 3 represents the closeness of the scatter points to the coordinates (1, 1). A higher regular shape index approaching 1 indicates a stronger resemblance of the particle's overall shape to that of a cube.

The classification of particle shape can be divided into two theoretical approaches: one focuses on length measurements, which involve parameters like elongation ratio and flatness ratio; the other is based on volume and surface area, which includes descriptors like true sphericity. These parameters encapsulate the extent to which a particle approximates certain regular shapes—be it elongated, flattened, or spherical—regardless of particle size. The sharpness of a particle's edges and corners is gauged by its roundness, which is an important characteristic. Additionally, sphericity and roundness are two separate morphological attributes that indicate different properties of a particle. Sphericity predominantly hinges on elongation, whereas roundness is considerably influenced by the angular protrusions' sharpness on an object. To summarize, Table 3 delineates the requisite parameters extracted from the point cloud to facilitate the computation of each morphological descriptor.

The parameter extraction process involves Python and Matlab programming to analyze scanning results and derive relevant information. During the processing phase, a triangular mesh is generated using three points that are closely located and serve as vertices. The computation of surface area involves the summation of the areas of all the triangular planes that are formed. Volume assessment employs the tetrahedral mesh method, involving the generation of tetrahedral meshes from the point cloud. Total volume results from the summation of all tetrahedral volumes within the ballast particles. Utilizing the trimesh toolkit in Python, the

**Table 2** Ballast morphology description parameters

Dimension	Parameter name	Formulas	Parameter implications
Form	Elongation ratio [5]	$\frac{S}{I}$	$L$ : Longest axis
	Flatness ratio [5]	$\frac{I}{L}$	$I$ : Intermediate axis
	Flat and elongation ratio [24]	$\frac{S}{L}$	$S$ : Short axis
	Flatness index [24]	$\frac{I+L}{2S}$	$S_s$ : Surface of a sphere with same particle volume
	True sphericity [23]	$\psi_s = \frac{S_s}{S_p}$	$S_p$ : Particle surface area
	Sphericity [23]	$\psi_v = \sqrt[3]{\frac{V_p}{V_c}}$	$V_p$ : Particle volume
	Intercept sphericity [29]	$\sqrt[3]{\frac{IS}{L^2}}$	$V_c$ : Volume of circumscribed sphere
	Corey shape factor [30]	$\frac{S}{\sqrt{LI}}$	$p$ : $S/I$
	Maximum projection sphericity [31]	$\sqrt[3]{\frac{S^2}{LI}}$	$q$ : $I/L$
	Working sphericity [32]	$\frac{12.8 \sqrt[3]{p^2q}}{1+p(1+q)+6\sqrt{1+p^2(1+q^2)}}$	$W$ : Sample weight
Roundness	3D roundness [25]	$R = \frac{\sum g(k)  k_{max} ^{-1}}{NR_{ins}}$	$n$ : Number of particles
	3D roundness [33]	$R_{3D} = \frac{r^{3D_i}}{NR_{ins}}$	$G_s$ : Specific gravity
	3D roundness [34]	$R = \frac{V}{S \sqrt[3]{abc}}$	$g(k)$ : Potential ‘corner’ at a given vertex on the surface
			$ k_{max} ^{-1}$ : Curvature radius
			$R_{ins}$ : Radius of the maximum inscribed sphere
			$r^{3D_i}$ : The radius of the $i$ th filling sphere obtained from the sphere-filling algorithm
			$N$ : Number of filling spheres

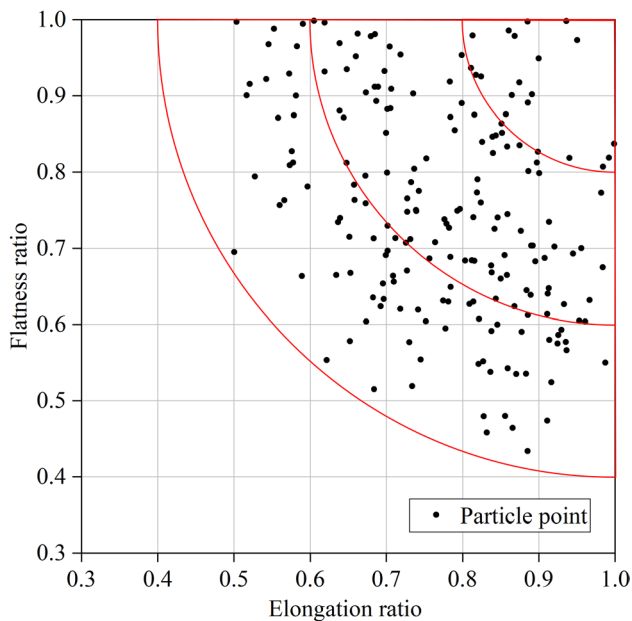


**Fig. 3** Ballast elongation ratio and flatness ratio distribution

minimum volume external rectangle and sphere are determined. From these, the lengths of the rectangle’s three sides, as well as the radius of the sphere, are deduced—representing the long, middle, and short axes of the ballast particles, and the minimum external sphere radius, respectively.

The proposed method utilizes a point cloud-based approach to estimate roundness, which is based on the

**Table 3** Point cloud extraction parameters

Parameter	Implications
$L$	Longest axis
$I$	Intermediate axis
$S$	Short axis
$V$	Volume
$S_s$	Surface area
$R_c$	Circumradius
$R_{in}$	Inscribed sphere radius
$R_{ac}$	Mean curvature radius of localized corners of the point cloud

roundness estimation approach developed by Nie [33], illustrated in Fig. 4. Initial uniform point cloud distribution on the particle surface occurs through a gridding process, eliminating redundant points at approximately 2 mm intervals, as shown in Fig. 4a, b. This step serves to reduce the impact of surface roughness on calculations. Following that, a specific point of interest is chosen on the surface of the particle as the target point. This point is then encompassed by 10 adjacent points, which are utilized for the purpose of extracting a local point cloud. At the target point, normal direction vectors extending outward from the particle surface are determined, as depicted in Fig. 4c. The sphere-filling technique is utilized to expand a sphere in the negative normal direction of the target point until it makes tangential contact with

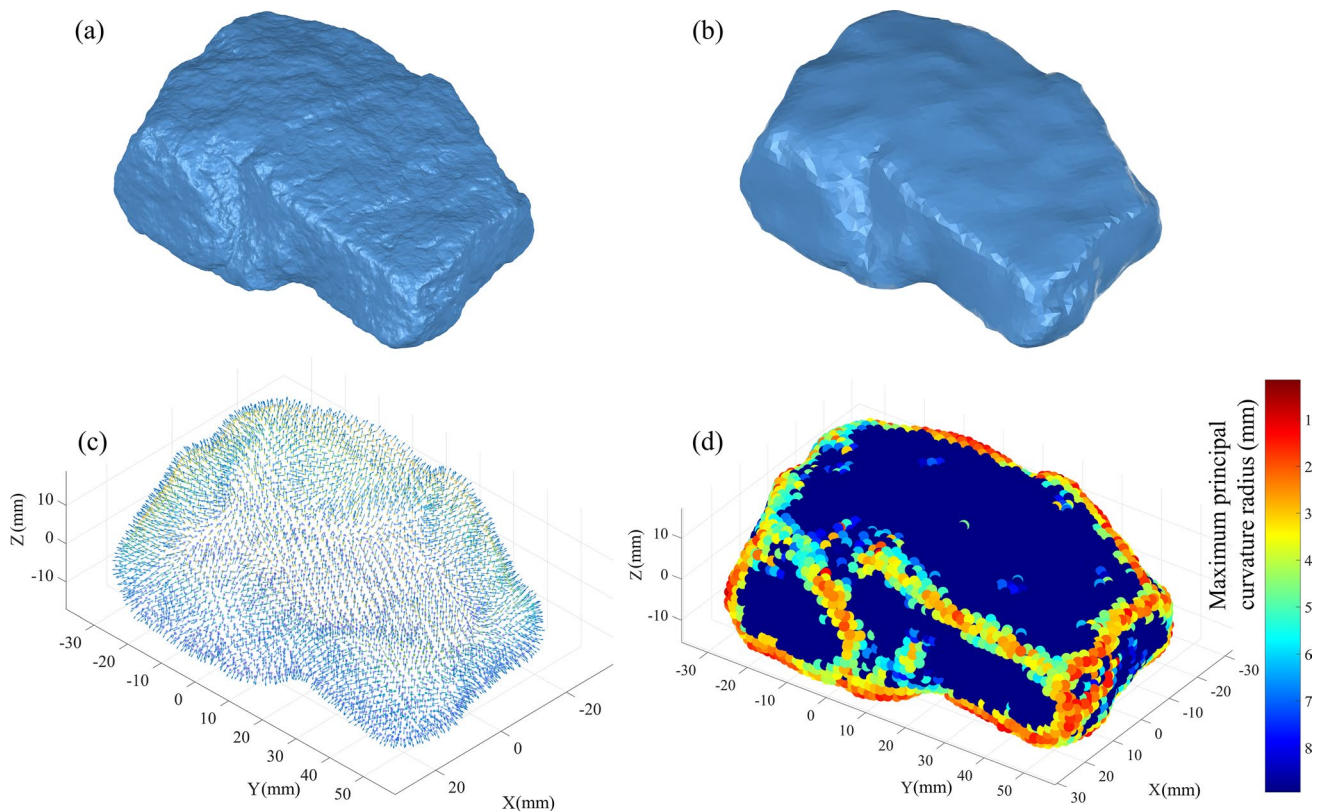


**Fig. 4** Calculation of the local inscribed sphere radius **a** ballast particle contour; **b** contour after gridded treatment; **c** normal vector of the point cloud; **d** distribution of the maximum principal radius of curvature

an auxiliary point. This sphere represents the local point cloud's inner tangent sphere, with its radius reflecting the maximum principal radius of curvature. In the event that the radius of this sphere is less than that of the inscribed sphere of the point cloud, it is possible to classify the local point cloud as either an edge or a corner. The adjustment process takes into account factors beyond the immediate vicinity, resulting in a reduction of the diameter of the inner tangent sphere. This reduction is carried out until all surface points of the particles are positioned either on or outside the sphere. The principal radius of curvature at particle corners is thus attained, shown in Fig. 4d. The average radius of all local inner tangent spheres is then computed.

The maximum inscribed sphere radius of the particle is determined using the following process, as illustrated in Fig. 5a. Extending distance field proposed by Cornea [35] to three dimensions, this field signifies the nearest distance from any interior point within the shape to its surface, as shown in Fig. 5b. The establishment of the first interior point is initiated by calculating the average coordinates of the surface point cloud. Then the process involves determining the coordinates of the nearest surface point. Additionally, the vector pointing from the interior point to the nearest surface point is also calculated. This vector's modulus serves as the

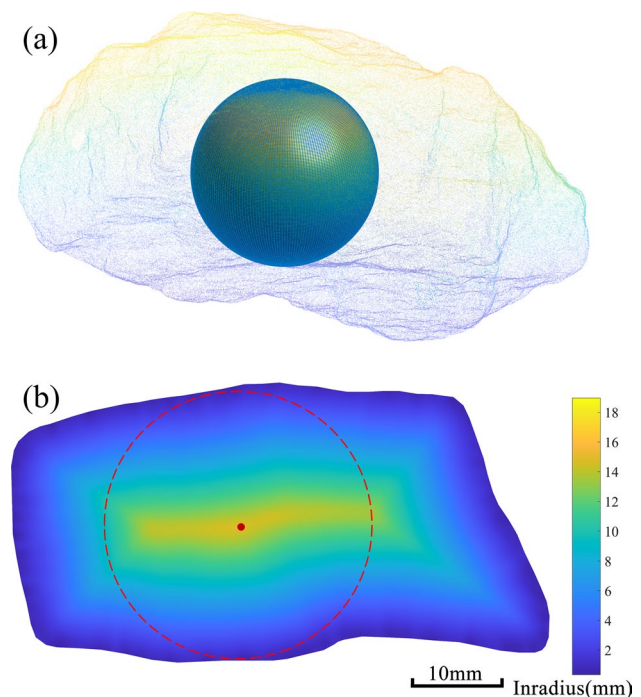


**Fig. 5** Calculation of the maximum inscribed sphere radius **a** inscribed sphere of the particle; **b** section of three-dimensional distance field

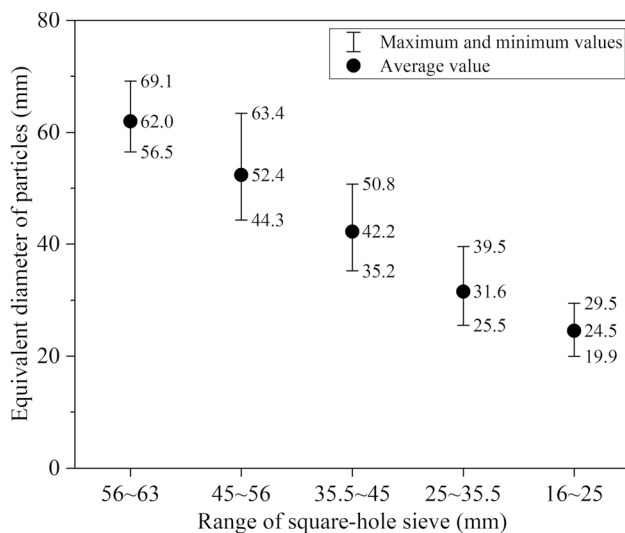


**Fig. 6** Equivalent grain size of ballast for each group

radius of the inscribed sphere centered at the interior point. Shifting this interior point to a specific distance in the opposite vector direction yields a new interior point. The iteration of the process continues until the modulus of the new vector is less than the modulus of the previous vector of the interior point, which is directed towards the nearest surface point, prior to being shifted. The interior point mentioned earlier serves as the center of the tangent sphere for the particle. The magnitude of the vector from this sphere center to the closest point on the surface determines the radius of the particle's maximum inscribed sphere. Particle roundness is computed using the three-dimensional Wadell roundness formula by Zheng [36], as depicted in Eq. (2).

$$R = \frac{R_{ac}}{R_{in}} = \frac{\sum_{i=1}^N r_i / N}{R_{in}} \quad (2)$$

In this equation,  $r_i$  denotes the radius of the inscribed sphere at the  $i$ th edge or corner.  $N$  represents the total count of inscribed spheres, and  $R_{in}$  signifies the radius of the maximum inscribed sphere.

The size of particle is a crucial factor that affects the strength of particle crushing [37–40]. Consequently, it indirectly influences the probability of particle crushing, which is an essential aspect considered in this study. For quantifying particle size, the equivalent diameter is adopted, representing the diameter of a sphere possessing an equivalent volume to the particle. Illustrated in Fig. 6, the mean equivalent particle size diverges by 10 mm across each particle group. It is worth noting that the range of particle sizes that are considered equivalent is in line with the spectrum of side lengths of square-hole sieves. The significance of the congruence lies in its emphasis on the role of equivalent

diameter in encapsulating the attributes of ballast particle size. This congruence highlights the relevance of equivalent diameter to engineering applications.

### 3.2 Ballast crushing mode and crushing strength

Figure 7 depicts three load–displacement curves that have been extracted from the test results. Due to the irregular shape and inhomogeneous internal structure of ballast particles, it is difficult to monitor the real stress–strain state inside the particles by experimental means like the unconfined uniaxial compression test used in this paper, so we alternatively analyzed the loading process based on the load–displacement curves and the characteristic stresses (calculated by dividing the load by the square of the equivalent diameter, similar to Eq. 4). The initial loading phase demonstrates a uniform elastic behavior observed in all three curves, providing evidence of adherence to the Hertzian elastic contact theory [17]. The contact between the particle and the platen is approximated as the contact between the sphere and the platen, and Eq. (3) is the equation for the relationship between load and displacement in the ball–plate contact process deduced from the Hertzian elastic contact theory, where  $\delta$  is the sphere deformation variable, equal to the upper platen displacement,  $R_0$  is the sphere radius, equal to half of the distance between the upper and lower platens,  $\mu_1, \mu_2$  and  $E_1, E_2$  are the Poisson's ratio and modulus of elasticity of the two contacting materials, respectively. According to the parameters of the test instrument, the Poisson's ratio of the upper and lower platens is 0.25 and the modulus of elasticity is  $2.06 \times 10^5$  MPa, and according to the parameters provided by the quarry, the Poisson's ratio of the granite parent rock is 0.17 and the modulus of elasticity is  $2.39 \times 10^4$  MPa. The Hertzian curves for each of the three particles were calculated based on the above parameters, as shown in Table 4. As shown in Fig. 7, the three particles have a segment of curves that overlap with the Hertzian curves at the beginning of loading, which indicates that they undergo a period of elastic loading, whereas as loading continues, the rock material's inherent brittleness leads to an impending breach of the yield point, causing the propagation of microfractures. As depicted in Fig. 7, point a, c and f denote the yield strength of the ballast [41]. Notably, at these points, the particles' load-bearing capacity remains considerably distant from their ultimate state. As the loading continues, the microfracture increases until it penetrates to form a macroscopic crack and the particles are crushed. The occurrence of transformation is highlighted by a sudden decrease in the load–displacement curve from its zenith. The peak point, such as point b in Fig. 7a, represents the ballast's crushing strength [42, 43]. In the test methods section, it is stated that overall crushing is only achieved if the particles are

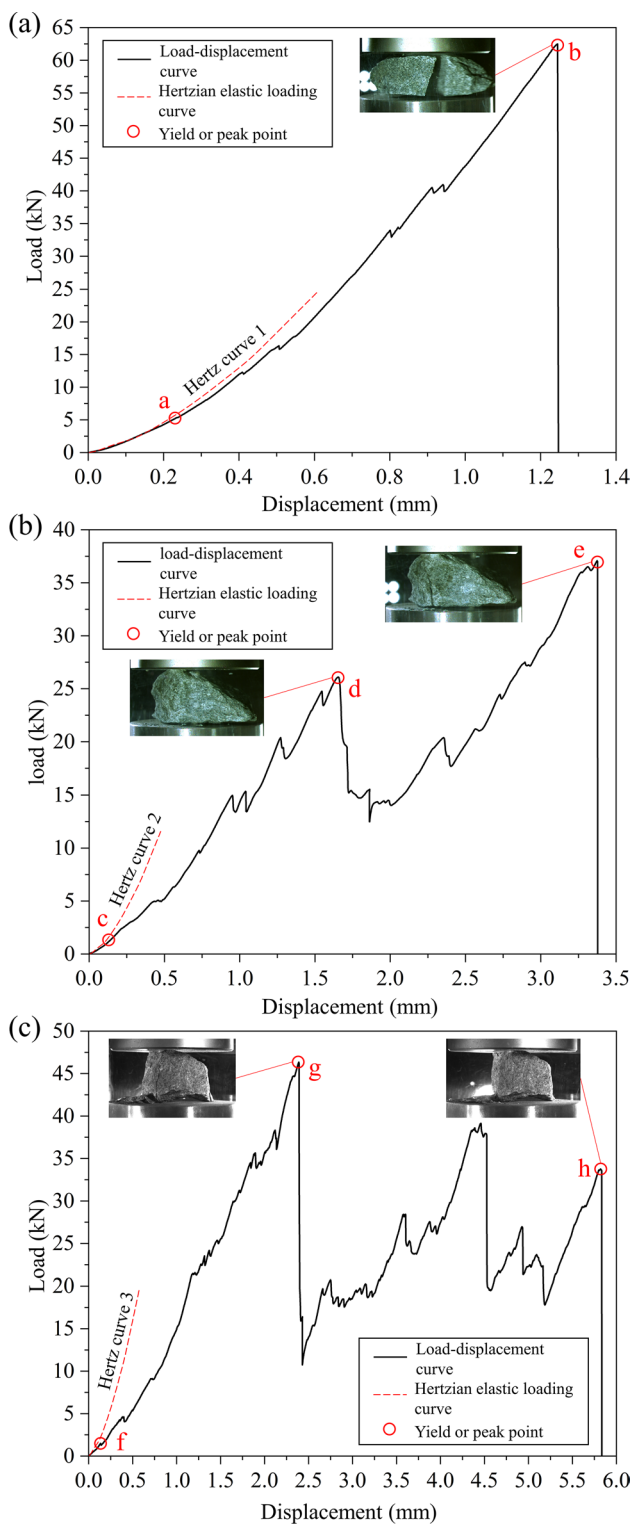


**Fig. 7** Load–displacement curves for different crushing modes **a** mode 1; **b** mode 2; **c** mode 3

crushed and the crushed mass reaches more than one third of the total mass, in such instances, the curve is similar to Fig. 7a, the peak point b corresponds to the overall

**Table 4** Hertz curve equation

Name	$R_0/mm$	Equation
Hertz curve 1	23.68	$P = 4.54 \times 10^9 \delta^{3/2}$
Hertz curve 2	22.17	$P = 4.39 \times 10^9 \delta^{3/2}$
Hertz curve 3	26.09	$P = 4.77 \times 10^9 \delta^{3/2}$

crushing strength of the ballast. On the other hand, if the initial crushing quality does not exceed the specified mass limit, only limited crushing will occur in a specific area, the curve is similar to Fig. 7b, where point d represents the localized crushing strength, then subsequent loading persists until overall crushing is reached. Of significance, the ultimate strength corresponds to the highest-load value during loading, identified at point e in Fig. 7b. For Fig. 7c, it has similar characteristics with Fig. 7b, i.e., the particles were crushed several times during the compression process, at the final peak point h, the mass of broken particles reaches one-third of the total mass and overall crushing occur, but unlike Fig. 7b, the maximum load of the particles appeared at the initial crushing, so for the particles of Fig. 7c, the point g at the initial crushing was chosen to calculate the ultimate strength to more closely reflect the compression resistance of the particles. The loading process of ballast particles can be decomposed into several stages, the elastic stage before the yielding point, and the elastic–plastic stage after the yielding. The elastic–plastic stage may be decomposed into several segments by the brittle damage, and each damage corresponds to a peak point. The yielding point and the peak point correspond to the yielding and crushing strengths, respectively, of which the maximum strength is called the ultimate strength. In this paper, ultimate strength will be used as a characterization parameter to analyze the ultimate bearing capacity of ballast particles. The compression and crushing of ballast particles are characterized by their inherent randomness. The stochastic nature of the crushing process is apparent in both the complex trajectory it follows and the variability observed in the resulting crushing strengths. Drawing a contrast with the established regularities observed in prior compression tests involving spherical particles [44, 45], the present study's observed irregularities can be attributed, in part, to the intricate and multifaceted geometry intrinsic to the complex structure of ballast particles.

$$\delta^3 = \frac{9}{2R_0} \left( \frac{1 - \mu_1^2}{E_1} + \frac{1 - \mu_2^2}{E_2} \right)^2 P^2 \tag{3}$$

The process of ballast crushing can be categorized into three distinct modes based on the number of crushing and



the ultimate strength. This categorization is illustrated in Fig. 7, where the diverse curves signify these modes. The complex interaction between the size, shape, and inherent defects of ballast grains stimulates the propagation of microcracks along different paths, resulting in a wide range of fracture locations. The first mode encompasses an initial rupture crack proximal to the particle center, yielding a sole intensity of fragmentation. The second mode entails a localized rupture that is limited to the contact area with the supporting plate, localized crushing has a small effect on overall strength, while ultimate strength corresponds to overall crushing strength. The third mode transpires through more uniform loading, the initial crack is further away from the particle's center, following localized crushing, the remaining intact portions foster additional internal microfractures, in this scenario, the ultimate strength is observed to arise from localized crushing, whereas the overall crushing strength is comparatively lower. The statistical analysis indicates that the first and second modes have a prevalence of approximately 45% each, these two modes play pivotal roles, while the third mode encompasses roughly 10%. The prominence of sharp corners precipitates stress concentration, rendering particles susceptible to localized crushing prior to overall fragmentation. The observed edge and corner lead to a higher occurrence of particles falling within Mode 2 and Mode 3, surpassing the count in Mode 1.

The determination of ballast strength was conducted utilizing the characteristic tensile strength calculation method introduced by Jaeger [46], as expressed in Eq. (4).

$$\sigma_f = \frac{F_p}{d^2}. \quad (4)$$

where  $\sigma_f$  is the characteristic strength,  $F_p$  is the load value corresponding to the ultimate strength, and  $d$  is the characteristic particle size of ballast, previous research has employed the uniaxial compression test's initial distance between upper and lower plates [14] or the average between the particles' maximum and minimum sizes [27] as the characteristic particle size. The equivalent particle diameter is selected as an appropriate parameter in this investigation.

The focus of this study is to provide a clear understanding of the relationship between particle morphology, size, crushing strength, and crushing probability. In order to mitigate the impact of particle defects, material disparities and surface joint, an effective approach is employed. In particular, ballast specimens originating from the same batch are carefully selected, ensuring that they are free from any noticeable surface joints. Augmenting this strategy, density analysis is integrated to identify particles significantly divergent from the average density value. Ballast density of every particle is computed by integrating mass measurements

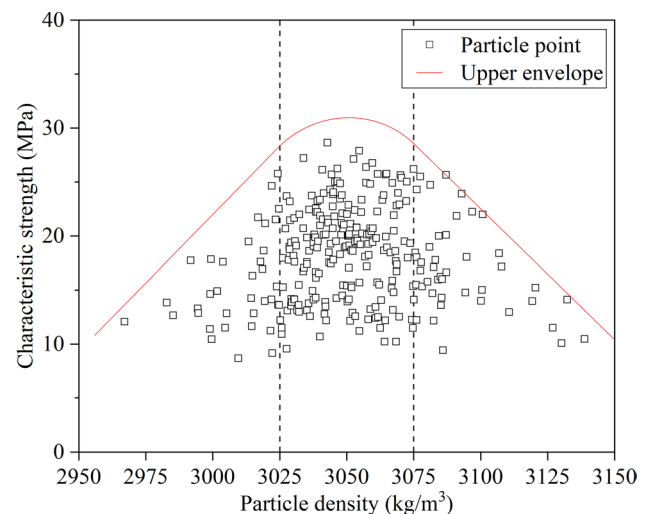


Fig. 8 Particle characteristic strength distribution with density

with volumetric assessments derived from morphological analysis. The calculated average density of the tested ballast material stands at 3050.6 kg/m<sup>3</sup>. Illustrated in Fig. 8, the characteristic strength distribution evinces uniformity across particles encompassing a density range of 3025–3075 kg/m<sup>3</sup>. The coherence observed in this system can be explained by the presence of similar internal fracture distributions and material compositions among particles that have comparable densities. Given the primary focus on scrutinizing particle morphology's impact, the testing scope is confined to ballast exhibiting densities within the 3025–3075 kg/m<sup>3</sup> range. This endeavor guarantees consistency in the internal composition of the ballast specimens being tested.

### 3.3 Impact analysis of particle morphology and size

The Spearman correlation analysis was utilized to identify the morphological parameters that have a significant impact on particle fragmentation. The results, presented in Table 5, elucidate the level of significance denoted by \*\* at the 0.01 level and \* at the 0.05 level. The data in the left column of the table are obtained according to the formula in Table 2. The ultimate crushing load in the upper column is the maximum load in the process of particle crushing, corresponding to the points b, e and g in Fig. 7, while the ultimate crushing displacement and ultimate characteristic strength are the displacement and characteristic strength of the particles under the ultimate load, respectively. To illustrate the process of obtaining Spearman's correlation coefficients with the examples of equivalent radius and ultimate crushing load in the table, it is known that there are 200 sample values for both variables, the sample values of the two variables are sorted and their ordinal numbers were recorded as  $x_i$  and  $y_i$ , and then  $x_i, y_i$  are brought into Eq. (5) to calculate the Spearman

**Table 5** Spearman correlation analysis

	Ultimate crushing load	Ultimate crushing displacement	Ultimate characteristic strength
Equivalent radius	0.863**	0.201**	− 0.448**
Elongation ratio	− 0.217**	0.150*	0.400**
Flatness ratio	0.124	0.213**	0.137
Regular shape index	− 0.068	0.291**	0.528**
Flat and elongation ratio	− 0.088	0.299**	0.495**
Flatness index	0.156*	− 0.251**	− 0.505**
True sphericity	− 0.232**	− 0.136	0.464**
Sphericity	0.078	0.122	0.360**
Intercept sphericity	0.008	0.302**	0.387**
Corey shape factor	− 0.168*	0.235**	0.498**
Maximum projection sphericity	− 0.168*	0.235**	0.498**
Working sphericity	− 0.102	0.289**	0.497**
Roundness	− 0.669**	− 0.336**	0.121*

correlation coefficient between the two variables. Where  $x_i$  and  $y_i$  are the corresponding ranking of the sample values of the two variables,  $\bar{x}$  and  $\bar{y}$  are the ranking average,  $n$  is the total number of sample values, and  $\rho$  is the Spearman correlation coefficient. Spearman correlation analysis in this paper is done with the aid of software IBM SPSS Statistics. The examination findings indicate that there are correlations between particle size and crushing load and strength. In contrast, the strength variation is primarily influenced by the overall shape of particles, while the impact of grain roundness is exerted on crushing load. With this insight, the analysis focused on the effects of specific morphological parameters, namely equivalent diameter, regular shape index, true sphericity, and roundness, on particle crushing parameters.

$$\rho = \frac{\sum_{i=1}^n (x_i - \bar{x})(y_i - \bar{y})}{\sqrt{\sum_{i=1}^n (x_i - \bar{x})^2 \sum_{i=1}^n (y_i - \bar{y})^2}}. \quad (5)$$

The previous section provided an in-depth analysis of ballast crushing modes during uniaxial compression testing, emphasizing the impact of particle morphology on these modes. As depicted in Table 6, the distribution of particles across different crushing modes within each group is illuminated. Mode 3, which accounts for approximately 10% of particles, maintains a consistently low level. On the other hand, modes 1 and 2 demonstrate a complementary relationship with reversing trends. The particle size decreases as the group number increases, as shown in Table 1. Correspondingly, the proportion of particles in mode 1 displays a declining-then-increasing trend, hitting a nadir at grain group 3, while mode 2 demonstrates the inverse pattern. The observed pattern indicates that particles with intermediate

**Table 6** Proportion of crushing modes for particles of different groups

Group number	Mode 1/%	Mode 2/%	Mode 3/%
1	50	40	10
2	35	52.5	12.5
3	32.5	60	7.5
4	42.5	50	7.5
5	60	30	10

sizes have a higher likelihood of undergoing localized fragmentation before experiencing overall crushing, while larger or smaller particles tend to undergo direct overall crushing without prior localized fragmentation.

The impact of the overall shape on the crushing mode is further investigated by analyzing the regular shape index and true sphericity value. The results of this analysis are presented in Table 7. As the regular shape index increases, the prevalence of particles in mode 1 demonstrates a decreasing tendency, with mode 2 displaying the opposite trend. The observed trend indicates a growing preference for localized fragmentation as the overall shape gradually becomes more cubic in nature. This trend peaks in the range 0.7–0.8. In contrast, the particle sphericity value's influence on the particle crushing mode is minimal, as indicated in Table 8. Consequently, the extent to which the shape of a particle resembles a square, as opposed to a sphere, has a significant impact on the pattern of fragmentation.

Furthermore, Table 9 underscores that the heightened roundness of particles, indicative of reduced corner sharpness, corresponds to a greater propensity for direct overall crushing (mode 1). Conversely, particles exhibit a tendency towards localized crushing when their roundness decreases.

**Table 7** Proportion of particle fragmentation modes with different regular shape index ranges

Regular shape index range	Mode 1/%	Mode 2/%	Mode 3/%
0.4–0.5	58.8	29.4	11.8
0.5–0.6	50	39.4	10.6
0.6–0.7	47.9	43.7	8.4
0.7–0.8	18.5	70.4	11.1
0.8–0.9	31.6	63.1	5.3

**Table 8** Proportion of particle crushing modes for different sphericity value ranges

Range of sphericity values	Mode 1/%	Mode 2/%	Mode 3/%
0.65–0.70	45.5	45.5	9
0.70–0.75	42.9	49	8.1
0.75–0.80	45	45	9
0.80–0.85	43.9	46.3	9.8

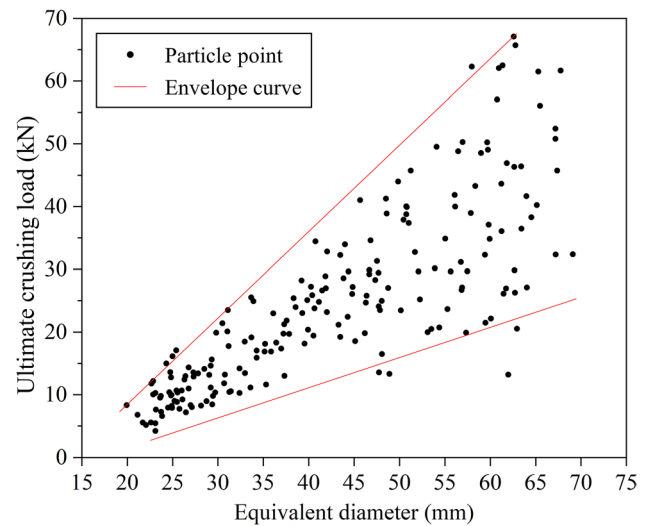
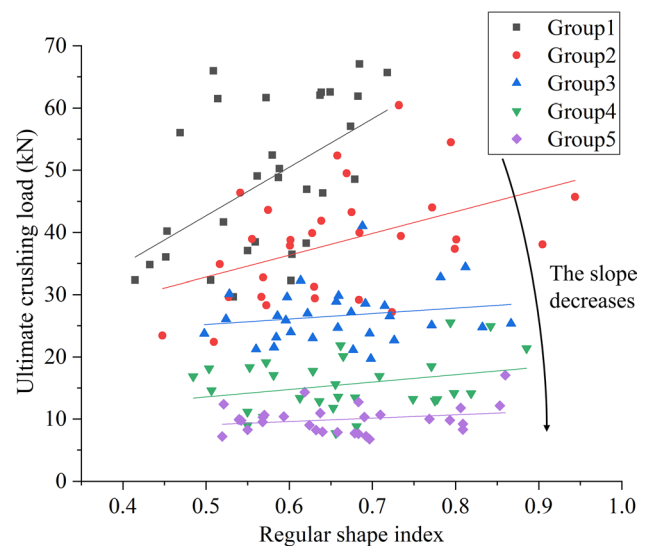
The phenomenon can be attributed to the protruding corners of particles, which facilitate increased contact with the plate. The presence of sharper corners results in the formation of stress concentrations, which in turn promotes localized fragmentation.

The determination of ultimate load is an important aspect of the crushing strength calculation process. It is influenced by factors such as particle size and morphology. As evident from Fig. 9, an increase in particle diameter corresponds to a rise in ultimate load during particle crushing. The observed correlation between larger particle diameters and enhanced load-bearing capability indicates a direct relationship, which aligns with the findings of previous researchers [12]. Furthermore, the expansion of ultimate load dispersion with growing particle size is evident. The observed phenomenon can be explained by the increased complexity of shape and internal structure in larger particles. This complexity results in a wider range of load-bearing capacities.

In the following analysis, we will now shift our focus to Figs. 10 and 11. These figures depict scatter plots that provide a visual representation of the relationship between ultimate load and two specific parameters: the regular shape index and the sphericity value. In order to maintain the consistency of observations within each group and minimize the impact of extreme values, a method is employed to exclude the five largest and smallest data points. This ensures the integrity of the observations by ensuring that each group consistently contains 30 data points. Notably, the impact of morphology on ultimate load exhibits variability across different particle sizes. As the regular shape index

**Table 9** Proportion of particle crushing modes with different roundness ranges

Roundness range	Mode 1/%	Mode 2/%	Mode 3/%
0.4–0.5	33.3	52.1	14.6
0.5–0.6	44.8	46.9	8.3
0.6–0.7	48.7	43.6	7.7
0.7–0.8	52.9	35.3	11.8

**Fig. 9** Grain size affects ultimate crushing load**Fig. 10** Regular shape index affects ultimate crushing load

and sphericity value increase, the ultimate load endured by particles also progressively rises. In essence, particles with morphologies closer to square or spherical forms exhibit heightened load resistance at equivalent particle size levels.

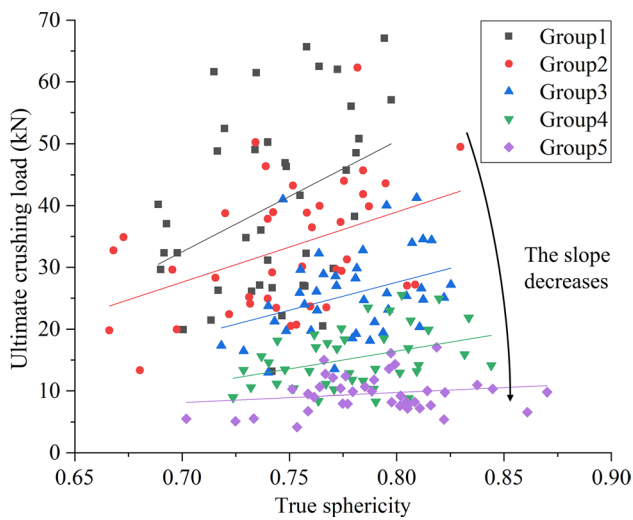


Fig. 11 True sphericity affects ultimate crushing load

Table 10 Correlation analysis between particle morphology and ultimate crushing load

	Group1	Group2	Group3	Group4	Group5
Spearman's correlation coefficient of regular shape index and ultimate crushing load	0.531**	0.438*	0.144	0.212	0.100
Spearman's correlation coefficient of sphericity value and ultimate crushing load	0.445*	0.321	0.275	0.148	0.108

Moreover, it can be observed that as the size of particles decreases, the impact of shape-based factors on ultimate load diminishes gradually, as indicated by the trend line slope approaching zero. The validation of this trend is demonstrated through the use of Spearman rank correlation coefficient analysis, as shown in Table 10. The correlation coefficient between ultimate load and the regular shape index or sphericity value decreases as the number of particle groups increases. This observation supports the idea that the influence of shape on ultimate load decreases as particle size decreases.

Figure 12 demonstrates a reduction in the maximum load that particles can withstand as their roundness increases. The average ultimate load is obtained by calculating the arithmetic mean of the ultimate loads of all particles in the corresponding roundness range. In accordance with Wadell's method for calculating roundness, as shown in Eq. (2), In the case of edge sharpness approximation, an increase in

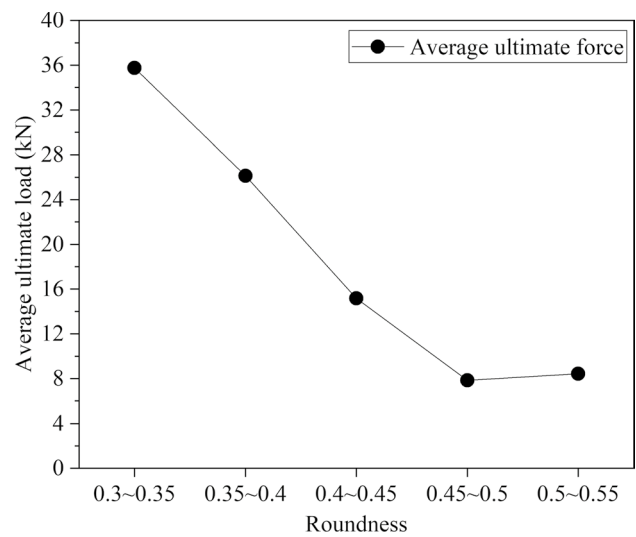


Fig. 12 Roundness affects average ultimate load

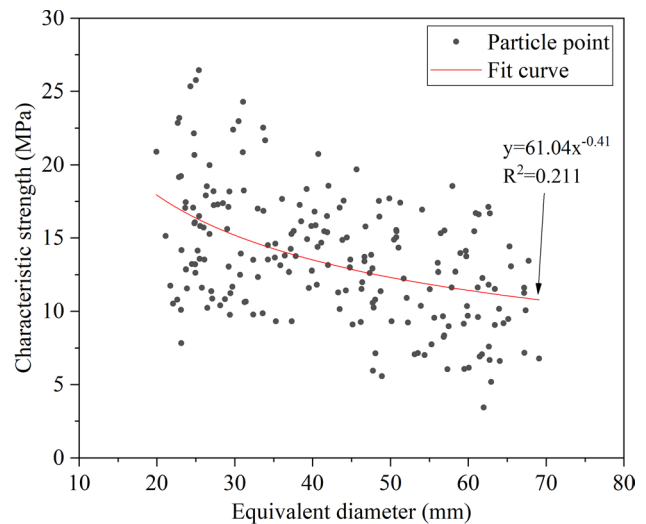
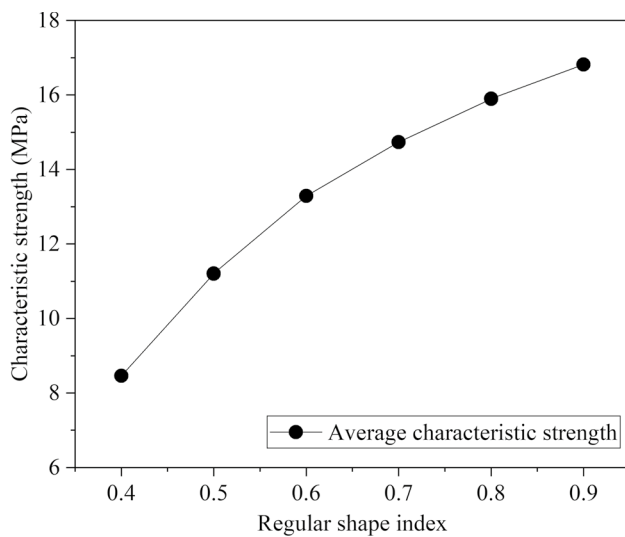


Fig. 13 Characteristic strength—equivalent particle diameter scatter plot

roundness results in a decrease in the size of the inscribed sphere. Consequently, particle size reduces, leading to reduced ultimate load as illustrated in Fig. 9. Simultaneously, when the inscribed sphere is reduced while maintaining a consistent particle volume, it results in a flattening of the particle shape. The flat particles have a compromised load-bearing capacity [19]. The convergence of these factors highlights the noted trend, as shown in Fig. 12.

Figure 13 exhibits a significant trend of decreasing characteristic strength of ballast particles with increasing equivalent diameter. The test results corroborate the relationship between particle strength and particle size posited by Lee



**Fig. 14** Trend of characteristic strength with regular shape index

[47] through the application of single-particle compression tests, as delineated by Eq. (6):

$$\sigma_f = Kd^b \quad (6)$$

In this equation,  $K$  represents a constant linked to the inherent material characteristics, while  $b$  stands as the size effect parameter. The fitted curves in Fig. 13 are in better agreement with Eq. (6), further indicating the size effect of ballast particles. During the compression test, ballast particles mostly split under longitudinal compression, and this process is mainly tensile damage, which is determined by the tensile capacity of the particles, so the characteristic strength calculated by Eq. (4) mainly reflects the tensile capacity of ballast particles. For a homogeneous and intact material, its tensile capacity is only related to the tensile strength of the material, which does not change with the change of size, but due to the effect of inhomogeneous lithology and microfractures inside the ballast particles, the particles are able to exert a tensile capacity that is less than the capacity of the material itself, and with the decrease of particle size, the lithology inside the particles tends to be homogeneous and the density of microfractures decreases, so its tensile capacity will gradually increase, and the corresponding characteristic strength will also increase, this law is in agreement with the simulation results of Scholtes [48]. Meanwhile, the particle points in Fig. 13 show greater dispersion, and the characteristic strengths of particles of similar sizes are not completely dependent on the fitted curves, which suggests that the characteristic strengths of the particles are also affected by other factors, such as the morphology of the particles.

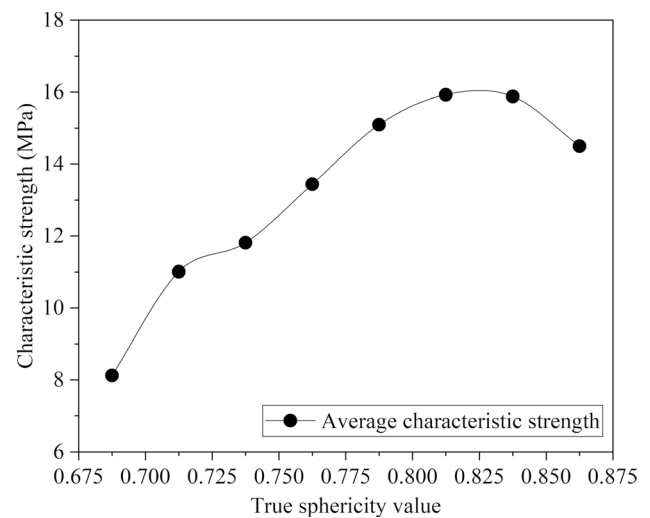


**Fig. 15** Trend of characteristic strength with true sphericity value

The objective of this part was to evaluate the impact of the regular shape index and the true sphericity value on the characteristic ballast strength. The characteristic strength demonstrates a gradual increase as the regular shape index of the particle increases, as depicted in Figs. 14 and 15. The average characteristic strength in the figure is obtained by calculating the arithmetic mean of the characteristic strengths of all particles in the range of the corresponding regular shape index or true sphericity values. This phenomenon arises from the tendency of a more square or spherical particle shape to distribute forces uniformly, thereby enhancing its capacity to withstand load for a given particle size. The particle strength is maximized when the sphericity value approaches approximately 0.825.

In summary, the crushing mode, ultimate crushing load, and characteristic strength of ballast are influenced by particle size and morphology. The complex morphological and dimensional characteristics of ballast particles lead to an increased discrete nature of their strength analysis compared to the regularly shaped specimens studied by others [44, 45].

### 3.4 Characteristic strength considering the effect of particle morphology

Equation (4) formulates the computation of characteristic strength by disregarding any influences beyond the particle size. However, as highlighted in the preceding section, particle morphology, as a dimension of apparent particle properties, exerts a substantial impact on particle behavior. Hence, we modify the simplified area  $d^2$  in Eq. (4) to the characteristic area  $A_c$ , accommodating shape characteristics. As a result, we introduce a new characteristic strength called the indirect characteristic strength  $\sigma_f$ . The discretization

inherent in strength analysis is mitigated by incorporating particle morphology factors into the strength calculation, as demonstrated in Eq. (7):

$$\sigma_I = \frac{F_p}{A_c} \tag{7}$$

Here  $A_c$  represents the characteristic area of the particle, which indicates the specific region that experiences stress during particle failure. To incorporate the combined effect of particle morphology, a morphological factor  $S_d$  is introduced in the original computation method, as delineated in Eq. (8):

$$A_c = d^2 \cdot S_d \tag{8}$$

During the process of determining the structure of  $S_d$ , four variables, namely equivalent radius, regular shape index, true sphericity value, and roundness, are subjected to principal component analysis. This analysis is performed to eliminate correlations among the variables and reduce the dimensionality of the data. It is worth noting that these variables play a significant role in influencing ballast crushing based on the previous analysis. The procedure unfolds in the following steps: Firstly, a  $200 \times 4$  matrix  $X$  is formulated, as portrayed in Eq. (9), where  $S_i$  represents the column vectors comprising each morphological parameter of the particles.

$$X = (S_1, S_2, S_3, S_4) \tag{9}$$

The column vectors are normalized to obtain the processed matrix  $X'$  by taking the mean of all the elements of each column subtracted from the individual elements and then divided by the corresponding standard deviation. as Eqs. (10) and (11).

$$S'_{ij} = \frac{S_{ij} - \frac{1}{n} \sum_{i=1}^n S_{ij}}{\sqrt{\frac{\sum_{i=1}^n (S_{ij} - \bar{S}_{ij})^2}{n-1}}} \tag{10}$$

$$X' = (S'_1, S'_2, S'_3, S'_4) \tag{11}$$

Subsequently, the covariance matrix  $Q$  of  $X'$  is computed, and its singular value decomposition is executed, as depicted in Eqs. (12) and (13), with  $U$  denoting the matrix containing  $Q$ 's eigenvectors, and  $\Lambda$  being the diagonal matrix incorporating the eigenvalues.

$$Q = \frac{1}{n} X'^T X' \tag{12}$$

$$Q = U \Lambda U^T \tag{13}$$

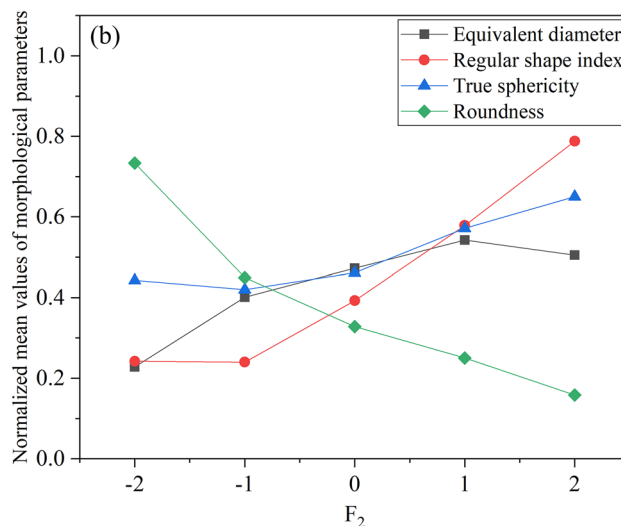
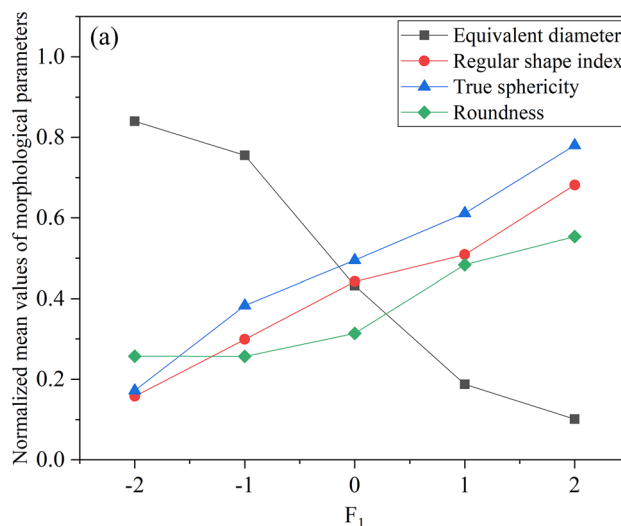


Fig. 16 Four morphological parameters versus  $F_1$  and  $F_2$  **a** Morphological parameters versus  $F_1$ ; **b** Morphological parameters versus  $F_2$

$$F = (F_1, F_2) = X' Y \tag{14}$$

$$Y = \begin{bmatrix} -0.600 & 0.257 \\ 0.420 & 0.626 \\ 0.547 & 0.301 \\ 0.407 & -0.672 \end{bmatrix} \tag{15}$$

The projection matrix  $Y$  is created by selecting the principal vectors corresponding to the two largest eigenvalues in  $\Lambda$ , using Eq. (14) and Eq. (15). Projection of matrix  $X$  onto these two principal vectors generates the principal factor matrix  $F$  after dimensionality reduction.  $Y$  represents the projection matrix, and the downscaled principal factor matrix explains 82% of information from the original matrix, with  $F_1$  and  $F_2$  being independent principal factor vectors

according to the results of principal component analysis obtained through the software IBM SPSS Statistics. Two independent variables  $F_1$  and  $F_2$  were extracted by eliminating the correlation between the four morphological parameters through the above principal component extraction process, which was ensured by the singular value decomposition of Eq. (13). As Fig. 16 exhibits the relationship between the four morphology parameters and  $F_1$  and  $F_2$ , where the vertical axis is the morphology parameter after the normalization process and averaged over the corresponding intervals. According to Fig. 16, variable  $F_1$  is negatively correlated with equivalent diameter and positively correlated with regular shape index, true sphericity, and roundness, while variable  $F_2$  is positively correlated with equivalent diameter, regular shape index, and true sphericity, and negatively correlated with roundness, which suggests that  $F_1$  and  $F_2$  have a strong correlation with the four morphology parameters, and that the above process of principal component extraction retains the key features of the four morphology parameters. Also  $F_1$  and  $F_2$  have completely opposite correlations in equivalent diameter and roundness, proving the independence between  $F_1$  and  $F_2$ .

Based on the analysis conducted, it is clear that there is a nonlinear correlation between morphology parameters and crushing parameters. As a result, the equations that describe the primary factors take the form of power exponents. An initial formulation is established, as demonstrated in Eq. (16). To ascertain the parameter values within this expression, both experimental data and the particle swarm intelligence optimization algorithm were employed for analysis, as documented in [49–51]. An approach aimed at achieving a coefficient of determination near 1, effectively minimizing discretization, was adopted. Additionally, to ensure practical relevance of the characteristic strength, the original characteristic strength's upper and lower limits were deployed as boundary conditions for the indirect characteristic strength. The process of determining the coefficients was carried out using Matlab programming. This process resulted in the formulation of each expression in Eq. (16), as explained by Eq. (17). Substituting Eq. (17) into Eqs. (7) and (8), the indirect characteristic strength was derived.

$$S_d = f(F_1) \cdot f(F_2) \quad (16)$$

$$S_d = F_1^{1.26} \cdot F_2^{-0.62} \quad (17)$$

It is shown that the characteristic strength calculation method has been improved due to the introduction of the morphology factor, by comparing Fig. 17 with Fig. 13, the correlation between the indirect characteristic strength and the equivalent particle size shows a stronger correlation than

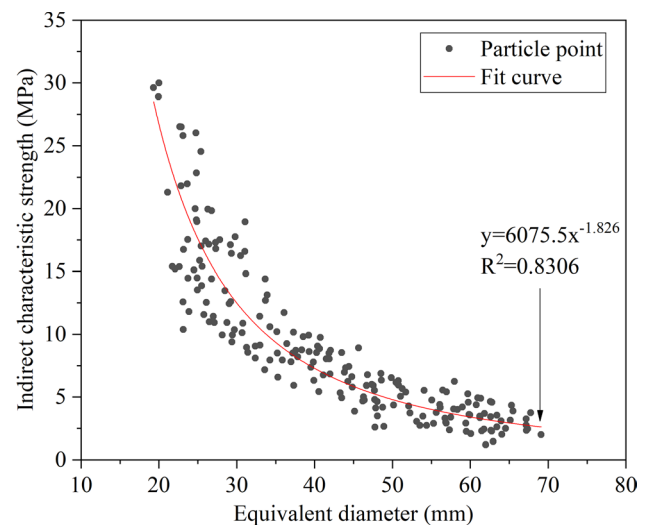


**Fig. 17** Indirect characteristic strength—equivalent particle diameter scatter plot

that between the characteristic strength and the equivalent particle size, and the relationship between the indirect characteristic strength and the equivalent diameter also satisfies Eq. (6). The coefficient of determination for the fitted curve surpasses 0.8, leading to a significant decrease in discretization during the strength analysis procedure.

### 3.5 Ballast crushing probability distribution model

The model is developed to predict the probability of ballast crushing in a single-grain compression test. This is done by utilizing the derived indirect characteristic strength as an intermediary and fitting test data. The connection between the indirect characteristic strength ( $\sigma_I$ ) and the characteristic crushing strength ( $\sigma_f$ ) can be established according to Eqs. (7) and (8), thus yielding Eq. (18).

$$\sigma_I = \frac{\sigma_f}{S_d} \quad (18)$$

As indicated by Fig. 17, a fitting relationship materializes between the indirect characteristic strength and the equivalent particle diameter, represented by Eq. (19).

$$\sigma_I = 6.075 \times 10^3 d^{-1.826} \quad (19)$$

$$P_s = \frac{i}{n+1} \quad (20)$$

Equation (20) outlines the methodology for computing the crushing probability ( $P_s$ ), which quantifies the probability of fragmentation occurring in individual ballast particles under the influence of uniformly distributed

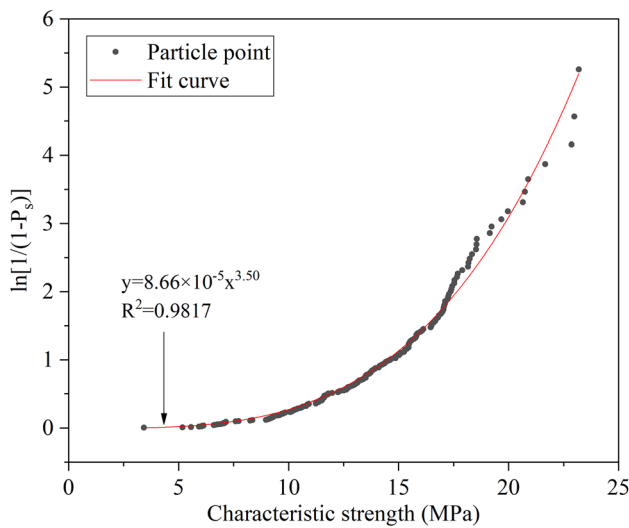


**Fig. 18**  $\ln[1/(1 - P_s)]$ —characteristic strength scatter plot

external forces. This formula presented here is designed to represent the combined characteristics of a given sample. In this formula, the variable “*i*” represents the sequential numbers assigned to individual particles, arranged in ascending order based on their ballast characteristic strengths. Additionally, the variable “*n*” denotes the total number of particles that have been tested. The relationship between the likelihood of fragmentation and the strength is modeled using the Weibull distribution, as illustrated in Fig. 18. The fitting outcome is formulated in Eq. (21) with an impressive coefficient of determination at 0.9817.

$$\ln\left(\frac{1}{1 - P_s}\right) = 8.66 \times 10^{-5} \sigma_f^{3.50} \tag{21}$$

With reference to Eqs. (18), (19), (20), and (21), the formula for predicting crushing probability is established in Eq. (22).

$$P_s = 1 - e^{-[8.66 \times 10^{-5} (6.075 \times 10^3 d^{-1.826} \times S_d)^{3.50}]} \tag{22}$$

Equation (22) represents the statistical correlation between the strength of particles, their morphology, and the probability of crushing. The equation allows for the estimation of the likelihood of ballast crushing, given the knowledge of the equivalent particle size, regular shape index, true sphericity value, and roundness degree.

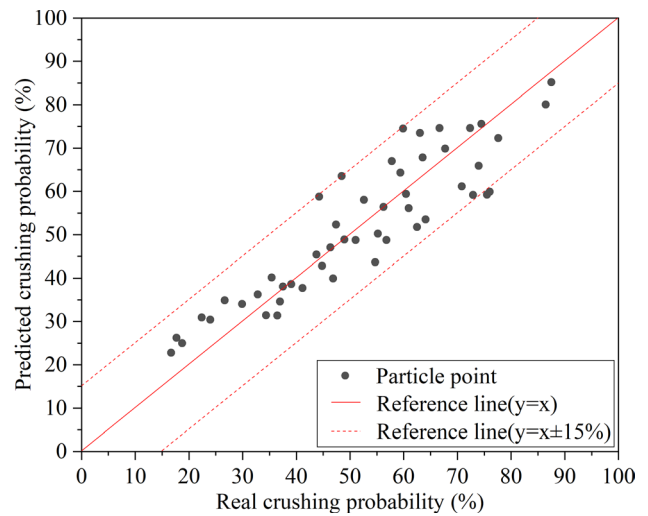


**Fig. 19** Scatterplot of predicted probability—true probability relationship considering the effect of particle morphology

### 4 Verification

A total of fifty ballast particles were selected at random, with ten particles chosen from each of the five distinct particle size groups. These particles were subjected to two different tests: 3D scanning tests and single-particle compression tests. These tests were conducted using identical conditions to those of the previous experiment. The fragmentation probabilities obtained from the tests were subsequently compared to the predicted outcomes. It’s noteworthy that the validation particle group maintained alignment with the original test

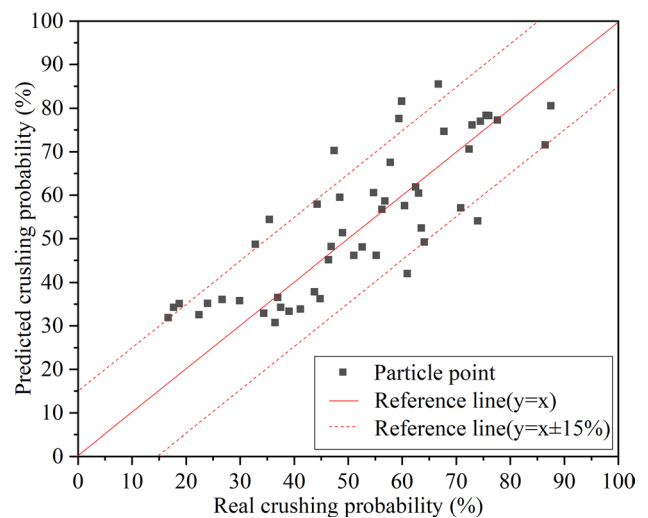


**Fig. 20** Scatterplot of predicted probability—true probability relationship without considering the effect of particle morphology



particle group concerning parameters such as particle size range, source of production, and density.

Figures 19 and 20 depict the prediction of fragmentation probability. When considering the impact of particle morphology, it was observed that 40 particles displayed prediction deviations in fragmentation probability within a range of 10%. Additionally, 10 particles exhibited prediction deviations ranging from 10 to 20%. In contrast, when particle morphology effects were not considered, there were 31 particles with fragmentation probability prediction deviations within 10%, 17 particles with prediction deviations from 10 to 20%, and 2 particles with prediction deviations exceeding 20%. The new model demonstrates an improved ability to make predictions. It is crucial to acknowledge that the reduced number of particles used in validation, as compared to the original test, results in each particle having a more pronounced influence on the overall outcome. Consequently, while computing the actual crushing probability, rather than reordering calculations as per Eq. (20), the characteristic strength is input into the test results to derive the true crushing probability via interpolation.

In the final analysis, this model takes into account both particle size and particle shape considerations. As a result, this method provides a higher level of accuracy in analyzing and predicting the crushing strength of particles. Additionally, it effectively represents the characteristic strength and crushing probability that are inherent to ballast particles.

## 5 Conclusion

In this paper, we describe the particle shape in terms of overall shape and roundness based on the scanning results, and we use the equivalent diameter to characterize the particle size based on the results of a series of three-dimensional scanning tests and single-particle compression tests on ballast. The ultimate crushing strength was chosen as the object of analysis after the characteristic crushing strength of various crushing modes was acquired through an examination of the load–displacement curves. The effects of different morphological and dimensional features, including equivalent diameter, regular shape index, true sphericity and roundness, on the crushing mode, ultimate crushing load and crushing strength are analyzed. Introducing the particle morphology index into the characteristic strength calculation is offered as a new approach that can reduce the dispersion in the strength analysis and produce more precise results. Weibull modeling with the updated characteristic strength as the medium is used to develop a model for the probability of a single particle being crushed in ballast. The paper has come to the following primary conclusions:

- (1) The fragmentation behavior is highly dependent on particle size. Overall fragmentation is more likely to occur in particles with big and small equivalent diameters, while localized fragmentation occurs first in particles with a medium equivalent diameter. The dispersion of ballast particles and the ultimate load they can withstand both rise as particle size grows. However, as particle size grows, the characteristic strength of ballast particles decreases.
- (2) The shape of the particles has a significant impact on how they break apart. Localized fragmentation precedes overall fracture because particles trend towards square or spherical forms. Although the effect diminishes with decreasing particle size, the ultimate load endurance of particles increases with increasing regular shape index. There is a positive relationship between characteristic strength and the regular shape index and the genuine sphericity value. The maximal load that particles can withstand falls as their roundness increases. Higher roundness leads to direct whole-particle crushing. Significantly, the effect of roundness on characteristic strength is negligible.
- (3) The proposed distribution model for fragmentation probabilities improves the precision of crushing probability analysis. With particle morphology in play, 29% more particles have forecast deviations of 10% or less, while 47% fewer particles have deviations of 10% or more. Better prediction is achieved when particle morphology is included in the model.

This paper provides an analytical method to analyze the effect of morphology and particle size on particle crushing performance under simple stress conditions, i.e., uniaxial compression conditions, and demonstrates the research significance and feasibility of quantitative analysis of the effect of morphology and particle size on particle crushing. It provides a theoretical basis for further research on the crushing probability model of ballast under real aggregate conditions, i.e., more complex stress conditions. Subsequently, based on the crushing probability model proposed in this paper, a discrete element single particle model will be established for aggregate test simulation to analyze the crushing mechanism of ballast particles from a fine perspective.

**Acknowledgements** This work was financially supported by National Natural Science Foundation of China (NSFC) (Grant Nos. 51878521, 51178358). The support is gratefully acknowledged.

**Data availability** Data will be made available on request.

## Declarations

**Conflict of interest** The authors declare that they have no known competing financial interests or personal relationships that could have appeared to influence the work reported in this paper.

## References

- Indraratna, B., Salim, W., Rujikiatkamjorn, C.: *Advanced Rail Geotechnology—Ballasted Track*. CRC Press/Balkema, Boca Raton (2011)
- Indraratna, B., Ngo, T., Rujikiatkamjorn, C.: Performance of ballast influenced by deformation and degradation: laboratory testing and numerical modeling. *Int. J. Geomech.* **20**, 04019138 (2020). [https://doi.org/10.1061/\(ASCE\)GM.1943-5622.0001515](https://doi.org/10.1061/(ASCE)GM.1943-5622.0001515)
- Lim, W.L., McDowell, G.R., Collop, A.C.: The application of Weibull statistics to the strength of railway ballast. *Granul. Matter* **6**, 229–237 (2004). <https://doi.org/10.1007/s10035-004-0180-z>
- Zhou, W., Yang, L., Ma, G., Chang, X., Lai, Z., Xu, K.: DEM analysis of the size effects on the behavior of crushable granular materials. *Granul. Matter* **18**, 64 (2016). <https://doi.org/10.1007/s10035-016-0656-7>
- Huang, Q.S., Zhou, W., Ma, G., Ng, T.T., Xu, K.: Experimental and numerical investigation of Weibullian behavior of grain crushing strength. *Geosci. Front.* **11**, 401–411 (2020). <https://doi.org/10.1016/j.gsf.2019.07.007>
- Zhang, X., Liu, X., Xu, Y., Wang, G., Zang, M.: Fragmentation modes of single coral particles under uniaxial compression: Microstructural insights. *Constr. Build. Mater.* **344**, 128186 (2022). <https://doi.org/10.1016/j.conbuildmat.2022.128186>
- Xiao, Y., Sun, Z., Desai, C.S., Meng, M.: Strength and surviving probability in grain crushing under acidic erosion and compression. *Int. J. Geomech.* **19**, 04019123 (2019). [https://doi.org/10.1061/\(ASCE\)GM.1943-5622.0001508](https://doi.org/10.1061/(ASCE)GM.1943-5622.0001508)
- Yan, W.M., Shi, Y.: Evolution of grain grading and characteristics in repeatedly reconstituted assemblages subject to one-dimensional compression. *Geotech. Lett.* **4**, 223–229 (2014). <https://doi.org/10.1680/geolett.14.00039>
- Xiao, Y., Liu, H., Chen, Y., Jiang, J.: Strength and deformation of rockfill material based on large-scale triaxial compression tests. I: influences of density and pressure. *J. Geotech. Geoenviron.* **140**, 04014070 (2014). [https://doi.org/10.1061/\(ASCE\)GT.1943-5606.0001176](https://doi.org/10.1061/(ASCE)GT.1943-5606.0001176)
- Liu, J.X., Sysyn, M., Liu, Z.Y., Kou, L., Wang, P.: Studying the strengthening effect of railway ballast in the direct shear test due to insertion of middle-size ballast particles. *J. Appl. Comput. Mech.* **8**, 1387–1397 (2022). <https://doi.org/10.22055/jacm.2022.40206.3537>
- Kalasin, T., Khamchan, C., Aoddej, A.: Effects of particle size and soil bed on the shear strength of materials in the direct shear test. *Period. Polytech.-Civ.* (2022). <https://doi.org/10.3311/PPci.20416>
- Xiao, Y., Meng, M.Q., Daouadji, A., Chen, Q.S., Wu, Z.J., Jiang, X.: Effects of particle size on crushing and deformation behaviors of rockfill materials. *Geosci. Front.* **11**, 375–388 (2020). <https://doi.org/10.1016/j.gsf.2018.10.010>
- Zhou, H.J., Ma, G., Yuan, W., Wei, Z.: Size effect on the crushing strengths of rock particles. *Rock Soil Mech.* **38**, 2425–2433 (2017). <https://doi.org/10.16285/j.rsm.2017.08.032>
- Zhao, X.L., Zhu, J.A., Jia, Y., Colliat, J.B., Bian, H.B., Zhang, Q.: Experimental and numerical study of size effects on the crushing strength of rockfill particles. *Int. J. Numer. Anal. Met.* **46**, 2060–2086 (2022). <https://doi.org/10.1002/nag.3379>
- Wang, Y.H., Ma, G., Mei, J.Z., Zou, Y.X., Zhang, D.R., Zhou, W., Cao, X.X.: Machine learning reveals the influences of grain morphology on grain crushing strength. *Acta Geotech.* **16**, 3617–3630 (2021). <https://doi.org/10.1007/s11440-021-01270-1>
- Zheng, S.F., Liu, Y., Zhang, N., Li, X., Gao, L.: Experimental studies on shape and size effects on particle breakage of railway ballast. *Transp. Geotech.* **37**, 100883 (2022). <https://doi.org/10.1016/j.trgeo.2022.100883>
- Aman, S., Tomas, J., Kalman, H.: Breakage probability of irregularly shaped particles. *Chem. Eng. Sci.* **65**, 1503–1512 (2010). <https://doi.org/10.1016/j.ces.2009.10.016>
- Kim, J., Park, B.S., Woo, S.I., Choi, Y.T.: Evaluation of ballasted-track condition based on aggregate-shape characterization. *Constr. Build. Mater.* **232**, 117082 (2020). <https://doi.org/10.1016/j.conbuildmat.2019.117082>
- Xu, Y., Yu, W.Y., Qie, L.C., Wang, H., Ning, N.: Analysis of influence of ballast shape on abrasion resistance using discrete element method. *Constr. Build. Mater.* **273**, 121708 (2021). <https://doi.org/10.1016/j.conbuildmat.2020.121708>
- Guo, Y.L., Markine, V., Song, J.N., Jing, G.Q.: Ballast degradation: effect of particle size and shape using Los Angeles Abrasion test and image analysis. *Constr. Build. Mater.* **169**, 414–424 (2018). <https://doi.org/10.1016/j.conbuildmat.2018.02.170>
- Jing, G.Q., Ji, Y.M., Qiang, W.L., Zhang, R.: Experimental and numerical study on ballast flakiness and elongation index by direct shear test. *Int. J. Geomech.* **20**, 04020169 (2020). [https://doi.org/10.1061/\(ASCE\)GM.1943-5622.0001791](https://doi.org/10.1061/(ASCE)GM.1943-5622.0001791)
- Danesh, A., Mirghasemi, A.A., Palassi, M.: Evaluation of particle shape on direct shear mechanical behavior of ballast assembly using discrete element method (DEM). *Transp. Geotech.* **23**, 100357 (2020). <https://doi.org/10.1016/j.trgeo.2020.100357>
- Wadell, H.: Volume, shape, and roundness of rock particles. *J. Geol.* **40**, 443–451 (1932)
- Blott, S.J., Pye, K.: Particle shape: a review and new methods of characterization and classification. *Sedimentology* **55**, 31–63 (2008). <https://doi.org/10.1111/j.1365-3091.2007.00892.x>
- Zhou, B., Wang, J., Wang, H.: Three-dimensional sphericity, roundness and fractal dimension of sand particles. *Geotechnique* **68**, 18–30 (2018). <https://doi.org/10.1680/jgeot.16.P.207>
- Weibull, G.W.: A statistical distribution function of wide applicability. *Appl. Mech.* **18**, 293–297 (1951)
- Al-Saoudi, N.K.S., Hassan, K.H.: Evaluation of indirect tensile strength of track ballast using weibull statistics. *Geotech. Geol. Eng.* **30**, 1097–1102 (2012). <https://doi.org/10.1007/s10706-012-9525-2>
- McDowell, G.R., Amon, A.: The application of Weibull statistics to the fracture of soil particles. *Soils Found.* **40**, 133–141 (2000). [https://doi.org/10.3208/sandf.40.5\\_133](https://doi.org/10.3208/sandf.40.5_133)
- Krumbein, W.C.: Measurement and geological significance of shape and roundness of sedimentary particles. *J. Sed. Petrol.* **11**, 64–72 (1941). <https://doi.org/10.1306/D42690F3-2B26-11D7-8648000102C1865D>
- Corey, A.T.: *Influence of Shape on Fall Velocity of Sand Grains*. Colorado A&M College, Colorado (1949)
- Sneed, E.D., Folk, R.L.: Pebbles in the lower colorado river, Texas a study in particle morphogenesis. *J. Geol.* **66**, 114–150 (1958). <https://doi.org/10.2307/30058239>
- Aschenbrenner, B.C.: A new method of expressing particle sphericity. *J. Sediment. Res.* **26**, 15–31 (1956)
- Nie, Z.H., Liang, Z.Y., Wang, X.: A three-dimensional particle roundness evaluation method. *Granul. Matter* **20**, 1–11 (2018). <https://doi.org/10.1007/s10035-018-0802-5>
- Hayakawa, Y., Oguchi, T.: Evaluation of gravel sphericity and roundness based on surface-area measurement with a laser scanner. *Comput. Geosci.-UK* **31**, 735–741 (2005). <https://doi.org/10.1016/j.cageo.2005.01.004>

35. Cornea, N.D., Silver, D., Min, P.: Curve-skeleton properties, applications, and algorithms. *IEEE Trans. Vis. Comput. Graph.* **13**, 530–548 (2007). <https://doi.org/10.1109/TVCG.2007.1002>
36. Zheng, J.X., He, H.T., Alimohammadi, H.: Three-dimensional Wadell roundness for particle angularity characterization of granular soils. *Acta Geotech.* **16**, 133–149 (2021). <https://doi.org/10.1007/s11440-020-01004-9>
37. Darlington, W.J., Ranjith, P.G., Choi, S.K.: The effect of specimen size on strength and other properties in laboratory testing of rock and rock-like cementitious brittle materials. *Rock Mech. Rock Eng.* **44**, 513–529 (2011). <https://doi.org/10.1007/s00603-011-0161-6>
38. Yu, Q.L., Zhu, W.C., Ranjith, P.G., Shao, S.S.: Numerical simulation and interpretation of the grain size effect on rock strength. *Geomech. Geophys. Geo-resour.* **4**, 157–173 (2018). <https://doi.org/10.1007/s40948-018-0080-z>
39. Skipochka, S., Krukovskiy, O., Palamarchuk, T., Prokhorets, L.: On the methodology for considering scale effect of rock strength. *Min. Miner. Deposits.* **14**, 24–30 (2020). <https://doi.org/10.33271/mining14.04.024>
40. Hu, G.J., Li, Y., Ma, G.: Research on the size effect of roughness on rock uniaxial compressive strength and characteristic strength. *Sci. Eng. Compos. Mater.* **28**, 613–627 (2021). <https://doi.org/10.1515/secm-2021-0058>
41. Antonyuk, S., Tomas, E., Heinrich, S., Morl, L.: Breakage behaviour of spherical granulates by compression. *Chem. Eng. Sci.* **60**, 4031–4044 (2005). <https://doi.org/10.1016/j.ces.2005.02.038>
42. Zhong, S., Baitalow, F., Nikrityuk, P., Gutte, H., Meyer, B.: The effect of particle size on the strength parameters of German brown coal and its chars. *Fuel* **125**, 200–205 (2014). <https://doi.org/10.1016/j.fuel.2014.02.022>
43. Dong, J., Cheng, Y.P., Hu, B., Hao, C.M., Tu, Q.Y., Liu, Z.D.: Experimental study of the mechanical properties of intact and tectonic coal via compression of a single particle. *Powder Technol.* **325**, 412–419 (2018). <https://doi.org/10.1016/j.powtec.2017.11.029>
44. Cheshomi, A., Mousavi, E., Ahmadi-Sheshde, E.: Evaluation of single particle loading test to estimate the uniaxial compressive strength of sandstone. *J. Petrol. Sci. Eng.* **135**, 421–428 (2015). <https://doi.org/10.1016/j.petrol.2015.09.031>
45. Zagar, G., Pejchal, V., Kissling, M., Mortensen, A.: On the diametric compression strength test of brittle spherical particles. *Eur. J. Mech. A-Solid.* **72**, 148–154 (2018). <https://doi.org/10.1016/j.euromechsol.2018.04.016>
46. Jaeger, J.C.: Failure of rocks under tensile conditions. *Int. J. Rock Mech. Min.* **4**, 219–227 (1967). [https://doi.org/10.1016/0148-9062\(67\)90046-0](https://doi.org/10.1016/0148-9062(67)90046-0)
47. Lee, D.M.: *The Angles of Friction of Granular Fills*. University of Cambridge, Cambridge (1992)
48. Scholtes, L., Donze, F.V., Khanal, M.: Scale effects on strength of geomaterials, case study: coal. *J. Mech. Phys. Solids* **59**, 1131–1146 (2011). <https://doi.org/10.1016/j.jmps.2011.01.009>
49. Petalas, Y.G., Parsopoulos, K.E., Vrahatis, M.N.: Memetic particle swarm optimization. *Ann. Oper. Res.* **156**, 99–127 (2007). <https://doi.org/10.1007/s10479-007-0224-y>
50. Beheshti, Z., Shamsuddin, S.M.H.: CAPSO: centripetal accelerated particle swarm optimization. *Inform. Sci.* **258**, 54–79 (2014). <https://doi.org/10.1016/j.ins.2013.08.015>
51. van Zyl, J.P., Engelbrecht, A.P.: Set-based particle swarm optimisation: a review. *Math.-Basel.* **11**, 2980 (2023). <https://doi.org/10.3390/math11132980>

**Publisher's Note** Springer Nature remains neutral with regard to jurisdictional claims in published maps and institutional affiliations.

Springer Nature or its licensor (e.g. a society or other partner) holds exclusive rights to this article under a publishing agreement with the author(s) or other rightsholder(s); author self-archiving of the accepted manuscript version of this article is solely governed by the terms of such publishing agreement and applicable law.